Regional Simulation of Intraseasonal Variations in the Summertime Hydrologic Cycle over the Southwestern United States

BRUCE T. ANDERSON

Department of Geography, Boston University, Boston, Massachusetts

(Manuscript received 10 April 2001, in final form 21 February 2002)

ABSTRACT

Using results taken from a finescale (25 km) regional modeling simulation for the summer of 1999, intraseasonal variations in the climatological summertime hydrologic cycle over the southwestern United States are described for two previously identified spatiotemporal precipitation patterns. Over the western portion of the Rocky Mountain plateau, centered on eastern Utah and western Colorado, columnar moisture divergence associated with precipitation is balanced by a combination of seasonal-mean convective moisture convergence and anomalous upper-air (>4 km) large-scale moisture convergence. The actual precipitating events themselves are predicated upon the anomalous upper-level advection of water vapor into the precipitating region; absent this large-scale advection at upper levels, vertical diffusion of moisture into the atmosphere balances large-scale divergence at midlevels, with little precipitation occurring. The anomalous large-scale advection during precipitating events is due primarily to anomalous large-scale vertical fluxes of moisture, with only a slight contribution from large-scale horizontal moisture fluxes. For precipitation located over the eastern portion of the plateau and the elevated orography of eastern New Mexico and southern Colorado, correlated moisture budget terms indicate that precipitation is again related to mean convective moisture convergence and anomalous midtroposphere large-scale moisture convergence. As with the western-plateau precipitation regime, this anomalous convergence is strongly correlated with an anomalous vertical advection of moisture; however, for the eastern-plateau regime, this vertical term is the sole source of large-scale moisture convergence contributing to rainfall in the region. In both cases, the vertical moisture convergence may be associated with previously identified intraseasonal modifications of the upper-level monsoon ridge centered over the Sierra Madre, which results in significant large-scale vertical velocities over the precipitating regions.

1. Introduction

The North American monsoon, and particularly its summertime southwestern branch, alternatively called the Mexican or Southwestern monsoon, has received much attention from the hydrologic and atmospheric community over the past years. In particular, the spatial, temporal, and spectral aspects of precipitation over the southwestern United States have been investigated on numerous scales using surface and satellite-derived observations of rainfall, outgoing longwave radiation, and lightning, as well as large-scale and finescale reanalysis and model simulation data (e.g., Stensrud et al. 1995; Schmitz and Mullen 1996; Petersen and Rutledge 1998; Comrie and Glenn 1998; Berg et al. 2000).

With regard to time, it has been shown that the mean intraseasonal timescale for wet and dry periods over Arizona is 2–4 days (Mullen et al. 1998), although the statistical spectral peak for these precipitation anomalies, along with those over the Great Plains region, is 12–18 days (Mullen et al. 1998; Mo 2000). This latter period is likely set by the advection timescale associated with the passage of midlatitude waves originating from the northern Pacific (Kiladis 1999; Mo 2000), suggesting a strong large-scale, midlatitude synoptic modulation of precipitation in this region (Carleton 1986; Stensrud et al. 1995; Maddox et al. 1995; Mo 2000).

With regard to space, there may be upward of nine separate *seasonal* precipitation regimes within the southern United States and northern Mexico (Comrie and Glenn 1998). Of interest, summertime precipitation over the monsoon regime, centered on New Mexico and eastern Arizona and extending along the Sierra Madre ranges in Mexico, can be further subdivided into four subregions; interannual variability in these four regions is associated with significantly different seasonal-mean 500-mb heights (Comrie and Glenn 1998), suggesting that different dynamic processes may be affecting these heterogeneous rainfall regimes. In addition, spatial heterogeneity in both simulated and observed summertime precipitation over the southwestern United States is found on intraseasonal timescales as well (Anderson and Roads 2002, hereinafter AR). At these timescales, rainfall can be decomposed into at least two predominant

Corresponding author address: Bruce T. Anderson, Dept. of Geography, Boston University, 675 Commonwealth Ave., Boston, MA 02215.
E-mail: brucea@bu.edu

intraseasonal precipitation regimes, one involving precipitation over the western portion of the Rocky Mountain plateau and another centered in the elevated regions of eastern New Mexico along the eastern slope of the plateau.

Previous investigations of the larger-scale synoptic conditions associated with precipitating and nonprecipitating periods in these two regions indicate that, in general, precipitating events are affected by dynamic processes within the midtroposphere, midlatitude monsoon environment (AR). It is of interest here to examine the atmospheric hydrologic fields associated with each of these intraseasonal precipitation regimes to determine how the synoptic-scale variations in the atmosphere produce the relevant hydrodynamic forcings that result in precipitation over the various regions. To examine these questions, simulation hindcasts from the National Centers for Environmental Prediction (NCEP) regional spectral model will be used along with daily precipitation observations taken from the National Climatic Data Center (NCDC) daily data archive. Section 2 describes the simulated and observed datasets. Section 3 outlines a systematic, analytical technique used to isolate well-simulated precipitation regimes within the modeling system; the hydrodynamic balances associated with these simulated regimes are then subsequently analyzed. Section 4 summarizes the results.

2. Datasets

a. Regional model description

The simulation of the summertime monsoon is performed using the NCEP regional spectral modeling system (Juang and Kanamitsu 1994; Juang et al. 1997). The NCEP global-to-regional modeling system used in this study contains two components—a low-resolution global spectral model (GSM) and a regional spectral model with a single nest (RSM). The nesting method is a one-way, noninteractive procedure that is designed to calculate regional responses (or adjustments) of the RSM to the large-scale background fields provided by the coarser-resolution GSM. This nesting procedure is performed through the entire domain, not only at the lateral boundary zones, and is therefore referred to as a perturbation method [see Juang and Kanamitsu (1994); Juang et al. (1997) for details]. Details of the full modeling system are found in the appendix.

The nesting described earlier allows the model system to capture the finescale features in the RSM, mainly because of enhanced orography of the study region, while still incorporating the development of large-scale synoptic features in the GSM. The resolution of the GSM is triangular-62 (approximately 200 km); the resolution for the RSM is 25 km $\times$ 25 km (Fig. 1). In the vertical, the prognostic equations are solved on 18 levels represented in sigma coordinates (where σ = pressure p divided by surface pressure p_s). The RSM domain extends from northern California to central Mexico and includes the Sierra Nevada and Rocky Mountain ranges in the United States, the Baja and Sierra Madre ranges in Mexico, and the Gulf of California. Also shown in Fig. 1 are selected radiosonde observing sites and binned precipitation locations (see below) used for evaluation of the simulated dynamic and hydrodynamic fields.

For this research, a ''continuous'' 92-day simulation is performed (see appendix), starting at 0000 UTC 1 July 1999. Prognostic and diagnostic output is archived every 6 model hours. The 6-h integrating intervals for all diagnostic terms (including precipitation) are 0000–0600, 0600–1200, 1200–1800, and 1800–0000 UTC; for this study, daily integrated values will be estimated from these 4-times-daily values. Research here will focus primarily on the various σ-level daily integrated diagnostic tendency terms. Of interest will be the regional simulations' budget terms for the water vapor tendency equation:

$$\frac{\partial q}{\partial t} + \left(\mathbf{v}\cdot\nabla q + \dot{\sigma}\frac{\partial q}{\partial \sigma}\right) + \left(P - g\frac{\partial E}{\partial \sigma}\right) = F,$$

where the three terms on the left represent the tendency, the total divergence, and precipitation minus vertical diffusion, and F is the residual forcing. Here q is moisture content (kg), t is time, $\mathbf{v}$ is the horizontal velocity vector, ∇ is the two-dimensional divergence operator, $\dot{\sigma}$ is the time-rate change of the vertical (sigma) coordinate, g is the acceleration of gravity, E is vertical eddy diffusion, P is precipitation, and F are the residual forcings. The residual forcings include horizontal diffusion, semi-implicit model adjustment, and boundary condition forcing. These three terms are typically small in the regions of interest; in general, the horizontal diffusion term serves to smooth finescale noise seen in the horizontal convergence term over regions of complex topography. The boundary condition forcing term can be large at the edges of the domain to account for large-scale forcing from the global model; however, this term is damped to zero within approximately 10 grid points of the edge. It should be noted that, for this paper, moisture divergence associated with the explicitly resolved vertical and horizontal advective fluxes of moisture will be referred to alternatively as large-scale divergence or simply divergence; the moisture divergence associated with vertical diffusion processes, related to the time rate of change of moisture due to parameterized subgrid-scale vertical motions in the model, will be referred to either explicitly as vertical diffusion or alternatively as eddy fluxes.

b. Surface and upper-air observations

To evaluate the regional model simulations, daily precipitation data from all stations in Arizona, New Mexico, Utah, and Colorado are taken from NCDC's daily

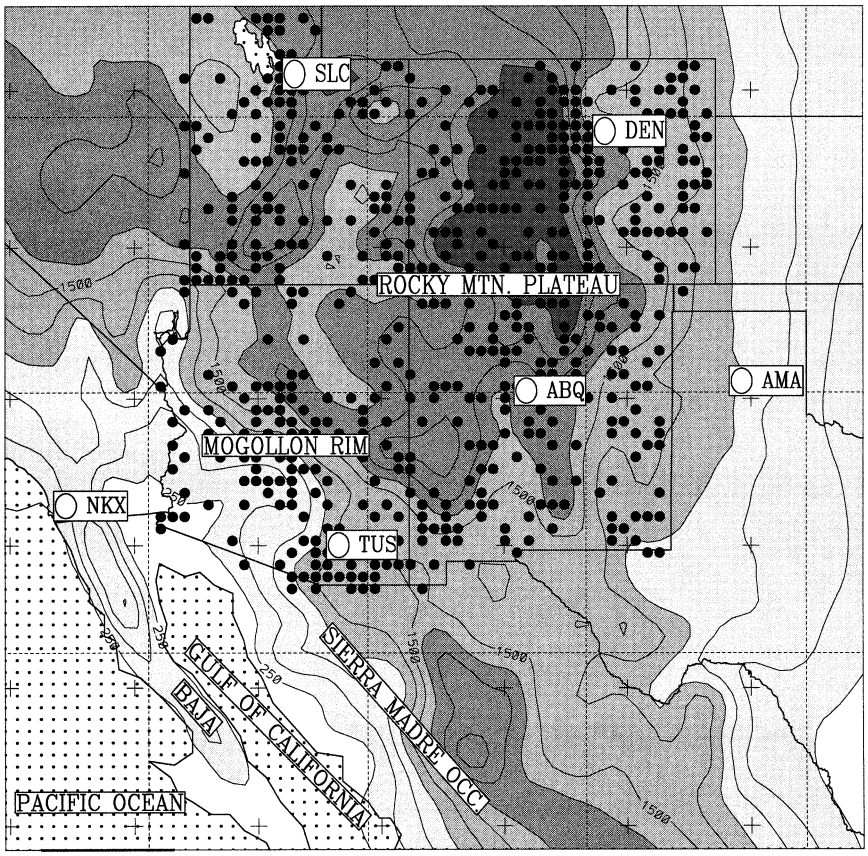

FIG. 1. RSM [• (25-km resolution), as seen over Pacific Ocean] and GSM [+ (T62)] grid points and RSM orography contours. Orography contour interval is 250 m; shading interval is 750 m with max shaded elev of 3000 m. Grid points for the binned obs precipitation sites are represented by filled circles (●). Location of important geographic and selected upper-air observing stations (○) are also shown: Tucson (TUS); Albequerque (ABQ); Amarillo (AMA); Denver (DEN); Salt Lake City (SLC); Miramar AFB, San Diego (NKX). Lat–lon lines are shown every 5°.

surface data archive for 1 July–30 September 1999. This station data are then averaged into 25 km × 25 km cells centered on the RSM grid points. To arrive at these binned values, the RSM grid points are used as center points for a 25-km square mesh. All station observations falling within a given mesh grid square are averaged together (with no geographic weighting or spatial interpolation), and the resulting value is assigned to the RSM grid point itself. Most grid points do not have a surface station associated with them. The majority of those that do have only one station located within their grid cell; the maximum number of stations per grid cell is three. This averaging ignores subgrid-scale effects associated with changes in elevation and surface characteristics (such as rain shadows); however, at the spatial scale of 25 km these effects are minimal given the spatial scale of the features of interest. For this study, missing data are treated as rain-free days; overall, missing data only constitute 1% of the total number of binned observations, and hence this approximation does not affect the results presented here.

3. Results

The NCEP regional spectral model has been used previously to identify, describe, and diagnose the dynamics of low-level summertime winds over the Gulf of California and the southwestern United States (Anderson et al. 2000a,b). In addition, finescale (25 km), regional modeling simulations, along with contemporaneous daily surface observations for the summer of 1999, have been used to identify and describe two robust spatiotemporal precipitation regimes for the southwestern United States (AR). Here, this research is extended to investigate the intraseasonal variability in the atmospheric hydrologic cycle associated with these precipitation regimes. Figure 2 presents the 3-month climatology of precipitation rates as seen in the full RSM simulation, RSM simulation data at the observation grid points, and surface observations themselves. Within the United States, all three indicate a precipitation maximum along a ridge running from southwestern New Mexico into northeastern New Mexico and extending

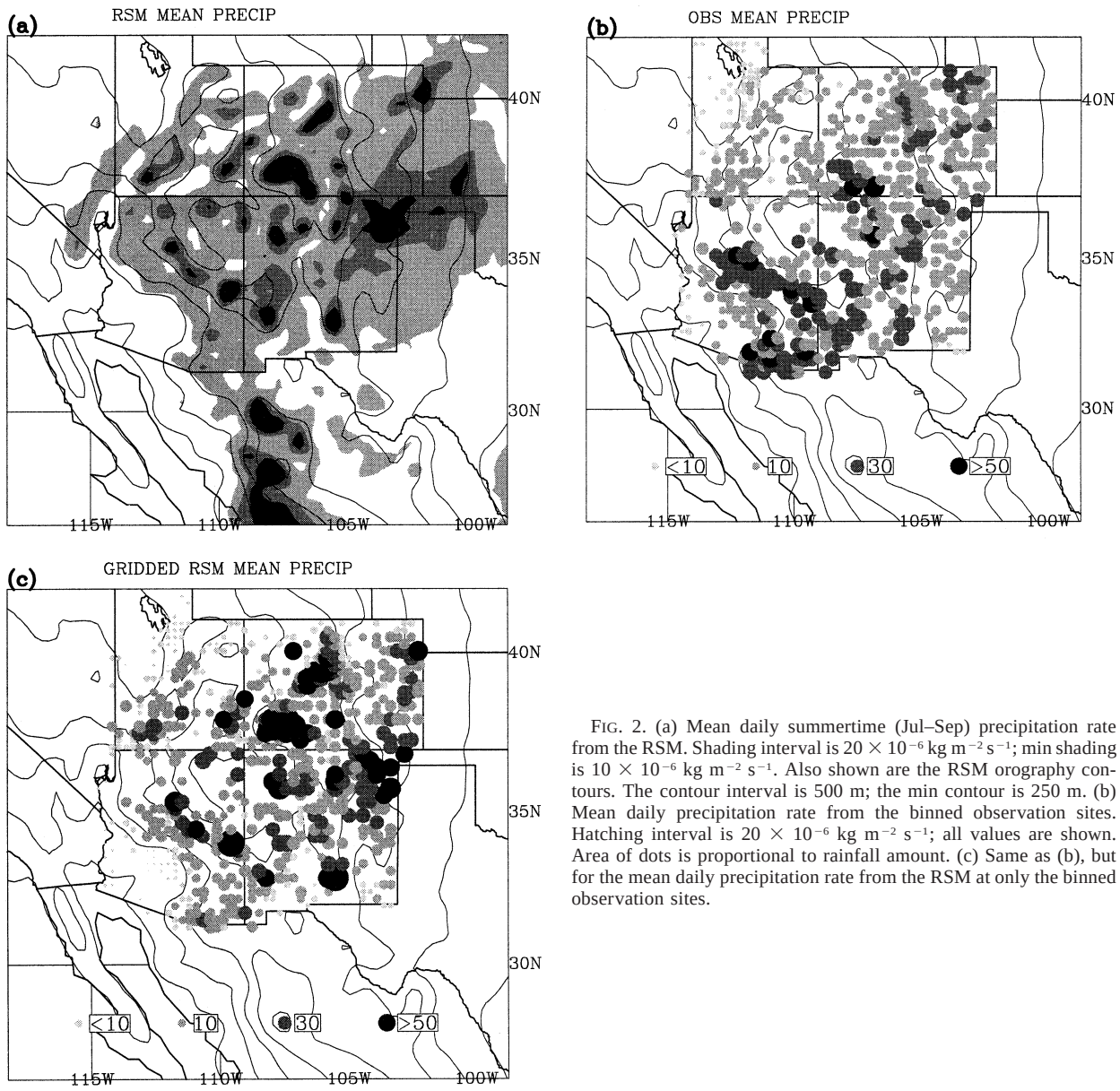

FIG. 2. (a) Mean daily summertime (Jul–Sep) precipitation rate from the RSM. Shading interval is 20×10^{-6} kg m^{-2} s^{-1}; min shading is 10×10^{-6} kg m^{-2} s^{-1}. Also shown are the RSM orography contours. The contour interval is 500 m; the min contour is 250 m. (b) Mean daily precipitation rate from the binned observation sites. Hatching interval is 20×10^{-6} kg m^{-2} s^{-1}; all values are shown. Area of dots is proportional to rainfall amount. (c) Same as (b), but for the mean daily precipitation rate from the RSM at only the binned observation sites.

into eastern Colorado, with additional maximums over the elevated regions of southwestern Colorado; the absolute maximum in the RSM product is found along the western side of the Sierra Madre Occidental. Minimum precipitation values tend to be found over southwestern Arizona and northwestern Utah. Overall, the two products show good agreement in magnitude and geographic structure, although the simulation indicates slightly too much precipitation over western Colorado and fails to capture the local maximums found along the Arizona–Mexico border (AR). However, it does capture the local maximums situated along the Mogollon rim in central Arizona.

Additional evaluation of the model simulations can be found in AR; here we only briefly review some of those results. In general, equitable threat scores (ETS) indicate that the model has skill, particularly over most of New Mexico, along the Mogollon rim, and also over eastern Colorado. In general, these equitable threat scores are of the same size as the typical Eta/reanalysis forecast ETS (between 0.15 and 0.25; Staudenmaier 1996; Chen et al. 1999; Hamill 1999), suggesting the model, although not perfect, is performing reasonably. Bias scores indicate that the model underestimates light precipitating events and overestimates the larger events ($>$15 mm day^{-1}). In general, the model tends to show a positive bias over eastern New Mexico, western Colorado and Utah; negative biases are principally found over southern Arizona. There is also statistical correlation between the simulated and observed gridpoint

precipitation values over the eastern portion of New Mexico and to a lesser extent over the Mogollon rim and central Utah, although the correlations are not extremely large (with correlation coefficients typically between 0.4 and 0.6).

Note, however, that these simple discrete statistics do not account for spatial and temporal structures in the fields themselves, which may be represented well by the model even if the individual gridpoint values are not. For instance, it has been shown that gridpoint estimation of precipitation based upon large-scale atmospheric circulation patterns results in low skill; however, there is a much stronger relationship between these same atmospheric circulation patterns and the geographical *distribution* of rainfall (Mamassis and Koutsoyiannis 1996). Evaluation of the *large-scale* temporal and spatial precipitation patterns within the simulations and observations, using rotated empirical orthogonal functions (EOFs) and canonical correlation algorithms (see below), indicates that the model has much better skill in simulating the major modes of spatial and temporal variability in precipitation for this region (AR). In addition, these results suggest that there is a strong regionalization of intraseasonal precipitation over the desert Southwest. All of those results will not be reproduced here. However, an analytic and systematic methodology designed to isolate those precipitation fields that the model is best able to simulate will be highlighted. These fields can then be used with some confidence to study the model dynamics and hydrodynamics to explain better the corresponding observed variability associated with these precipitation patterns.

To isolate these modes of covariability within the simulated/observed system, a simple canonical correlation analysis (CCA) is performed between the observed and simulated daily fields; this analysis entails minimizing the variance between the observed and simulated data products to produce a set of canonical factor (CF) time series sorted by descending covariance explained (as opposed to variance explained as in the case of principal component analysis). The observed and simulated precipitation datasets are first transformed by raising the absolute fields (as opposed to the anomalies) to the 1/5 power, thereby reducing the non-Gaussian nature of daily precipitation time series (Comrie and Glenn 1998). Next, the EOFs for each transformed dataset are computed. To examine only the largest modes of variability within the two systems, a subset of these EOFs (the first nine for the simulated precipitation fields and the first eight for the observed precipitation fields) are selected for use in the CCA algorithm. The next step in performing the CCA is to calculate the covariance matrix between the predictor, in this case the time series of simulated EOFs, and the predictand, that is, the time series of observed EOFs (the same procedure can be performed with the designations reversed and there is no loss of generality). The autocorrelation matrix for each of the fields is also required; because the time series of the EOFs are used, this autocorrelation matrix is simply a diagonal matrix that normalizes the values in the covariance matrix. A single value decomposition is then performed on a modified version of the covariance matrix, which produces a diagonal matrix of eigenvalues (equal to the squared correlation of the reconstructed time series) and a transformation matrix. The transformation matrix is used to reconstruct the time series of the CFs from the original temporal principal components. The corresponding spatial patterns are derived by equating the reconstructed CF-based anomaly field with the anomaly field represented by the original EOFs and then solving for the spatial loadings. The resultant time series are then normalized such that their inner products (as opposed to their variances) are unity. The spatial patterns are divided by the collocated standard deviations to arrive at spatial maps of correlation coefficients. By construction, the canonical factor time series for a given field are orthogonal to one another, although the spatial patterns are not necessarily so. See AR for further details.

Figure 3 shows the first CF spatial patterns of the simulated and observed precipitation, along with the corresponding time series, as derived via canonical correlation. As suggested previously, the time series for the two fields are correlated well (correlation coefficient r is 0.87), although this result is to be expected. For this factor, there are collocated precipitation correlation patterns over northern Arizona, eastern Utah, and western Colorado. This pattern qualitatively resembles a previously identified western plateau precipitation regime isolated using the independent rotated EOF fields (AR), although the pattern isolated via the CCA algorithm is situated further north, indicating better simulation by the model of precipitation in this region than over southern Arizona and the Mogollon rim. However, the fact that there is qualitative agreement between the spatial (and temporal) features isolated via the CCA algorithm and those isolated via the rotated EOF algorithm indicates that the model is indeed successfully simulating one of the predominant modes of variability in the observed system.

Figure 4 shows the same fields but for the second canonical factor. Again, the time series are correlated well ($r = 0.84$); they indicate strong precipitation events in the middle of July and at the beginning of August, with smaller events seen at the beginning of July and at the beginning and middle of September. The spatial patterns are characterized by maximum precipitation correlations over eastern New Mexico and eastern Colorado, similar to that seen for a previously identified eastern plateau precipitation regime (AR). As before, the spatial (and temporal) patterns suggest that this mode of variability is effectively captured by the modeling system.

Note that by including additional EOF components within the CCA algorithm, it is possible to isolate secondary patterns within the observed and simulated systems, which, although they do not explain much vari-

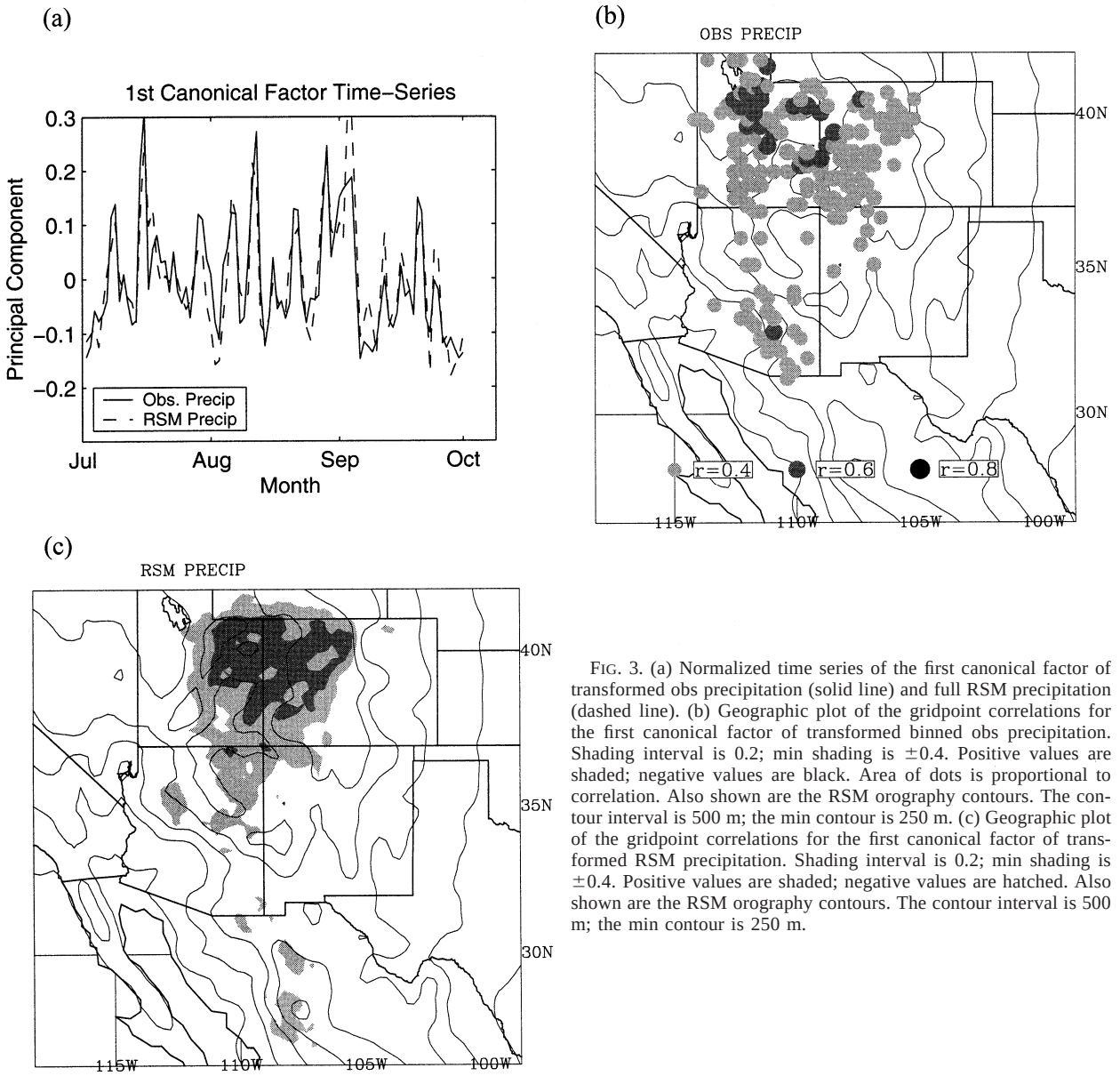

FIG. 3. (a) Normalized time series of the first canonical factor of transformed obs precipitation (solid line) and full RSM precipitation (dashed line). (b) Geographic plot of the gridpoint correlations for the first canonical factor of transformed binned obs precipitation. Shading interval is 0.2; min shading is ±0.4. Positive values are shaded; negative values are black. Area of dots is proportional to correlation. Also shown are the RSM orography contours. The contour interval is 500 m; the min contour is 250 m. (c) Geographic plot of the gridpoint correlations for the first canonical factor of transformed RSM precipitation. Shading interval is 0.2; min shading is ±0.4. Positive values are shaded; negative values are hatched. Also shown are the RSM orography contours. The contour interval is 500 m; the min contour is 250 m.

ance, may have well-correlated features. However, we found that the first two modes of variability seen here are the predominant two canonical factor modes when including anywhere from 5 to 15 EOFs in the CCA technique, suggesting that the higher components, although important for modifying the particular structure of the precipitation patterns, do not affect its overall large-scale features. Because of subjective considerations, we have decided to base our results here on the inclusion of nine simulated EOFs and eight observed EOFs. If we further increase the number of included EOFs through 35, we find that the best correlated modes shift to finescale structures within the model and observations; however, the two modes here are still represented in the first five canonical factors, indicating that they remain well correlated even when including numerous finescale structures within the CCA algorithm. To avoid isolating, and analyzing, too many disparate modes of finescale variability, we have instead decided to focus on just the larger-scale synoptically forced modes and have therefore reduced the number of included EOFs. Note also that the following analysis has been repeated using the canonical factors as derived from a previously published number of included EOFs (i.e., five for both simulated and observed datasets; see AR), and all results are quantitatively and qualitatively the same.

Now the hydrologic fields associated with these modes of variability will be investigated and the balances that lead to the subsequent simulated (and ob-

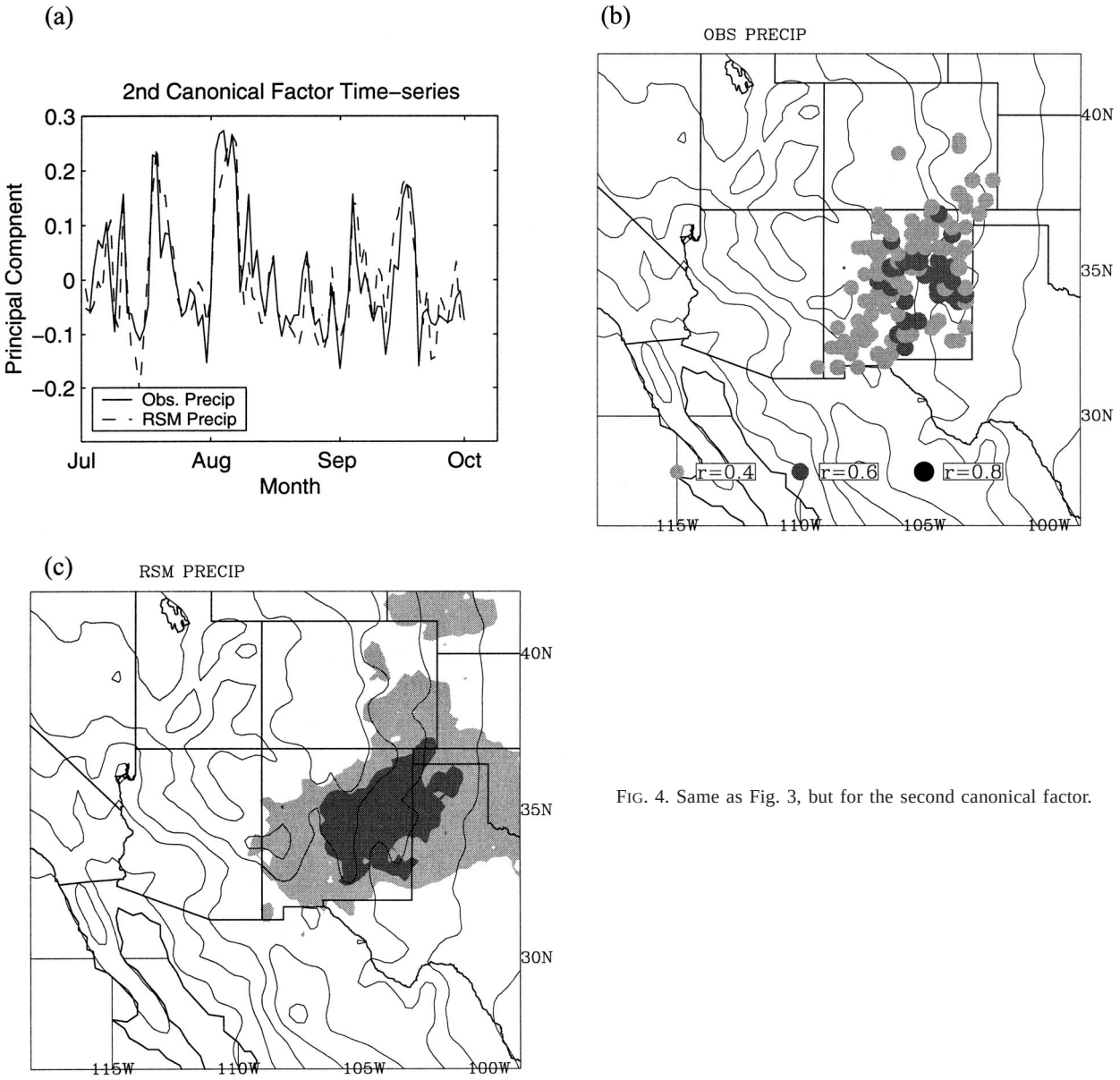

FIG. 4. Same as Fig. 3, but for the second canonical factor.

served) rainfall will be examined. As mentioned earlier, the modeling system archives the budget terms for the water vapor tendency equations throughout its integration. The climatology of these vertically integrated moisture budget terms is presented in Fig. 5. In the model simulation, the precipitation over the Sierra Madre Occidental, extending up into Arizona and western New Mexico, is predominantly associated with deep convection, with little contribution from either large-scale (e.g., explicitly resolved) precipitation or shallow convection. Over the elevated plains regions of eastern Colorado and western Kansas, this influence lessens and the predominant precipitation mechanism probably is related to large-scale dynamic forcing. In agreement with most studies of long-term mean hydrologic cycles, the water storage through the summer (as represented by the tendency term) goes to zero. Hence, on a climatological basis, the precipitation fields are balanced by the vertical diffusion of moisture into the column via evaporation and large-scale moisture convergence via dynamic transport. For the desert Southwest, the entire region has a large, negative vertical diffusion component (representing evaporative fluxes of moisture to the atmosphere) throughout the summer season; largest values are found over the northern Gulf of California, in agreement with previous studies (Berbery 2001). The northern gulf also represents the region of greatest large-scale moisture divergence. In addition, weak moisture divergence is found over most of the domain; in precipitating regions, moisture divergence is typically neg-

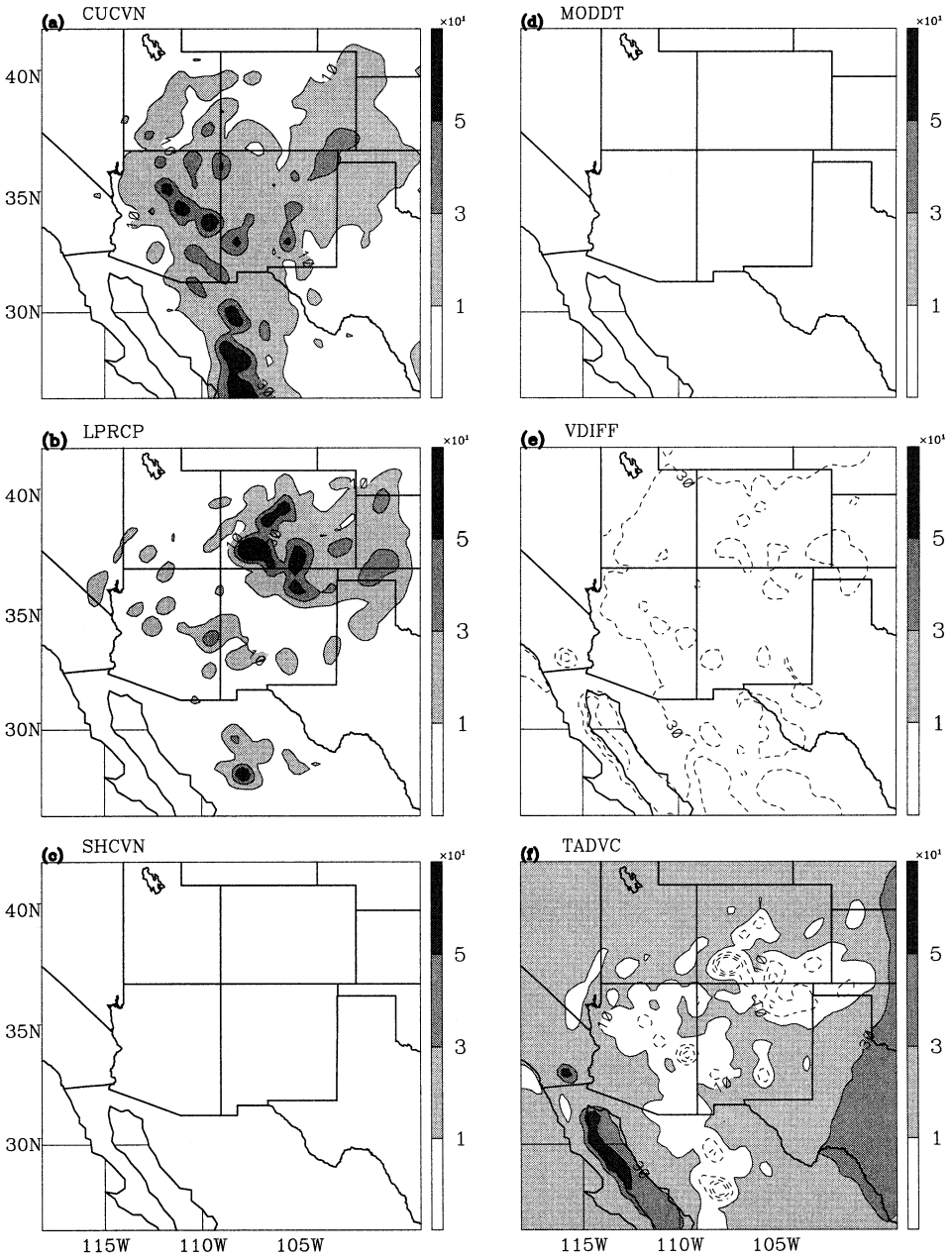

FIG. 5. Mean daily summertime (Jul–Sep) vertically integrated RSM diagnostic moisture tendency terms. Shading interval is 20×10^{-6} kg m^{-2} s^{-1}; min shading is 10×10^{-6} kg m^{-2} s^{-1}. Shown are (a) convective precipitation, (b) large-scale precipitation, (c) shallow convective precipitation, (d) moisture tendency, (e) vertical diffusion moisture divergence, and (f) large-scale total moisture divergence.

ative, although its magnitude is small except in very localized areas.

To study the full hydrologic cycle associated with the two previously discussed modes of intraseasonal variability, the first two CF time series of simulated precipitation, as derived via CCA with the observed fields, are correlated with the moisture tendency budget terms. As mentioned above, the CF time series are used because they correspond to the observed patterns that the model is best able to simulate, allowing one to use the value-added knowledge of the model dynamics and hydrodynamics to explain observed variability in the system. Figure 6 shows weighted covariance maps of the vertically integrated moisture budget terms for the first canonical factor. These values are calculated by taking the inner product of the normalized canonical factor time series with the daily anomaly values of the hydrologic budget terms at each grid point, then dividing by

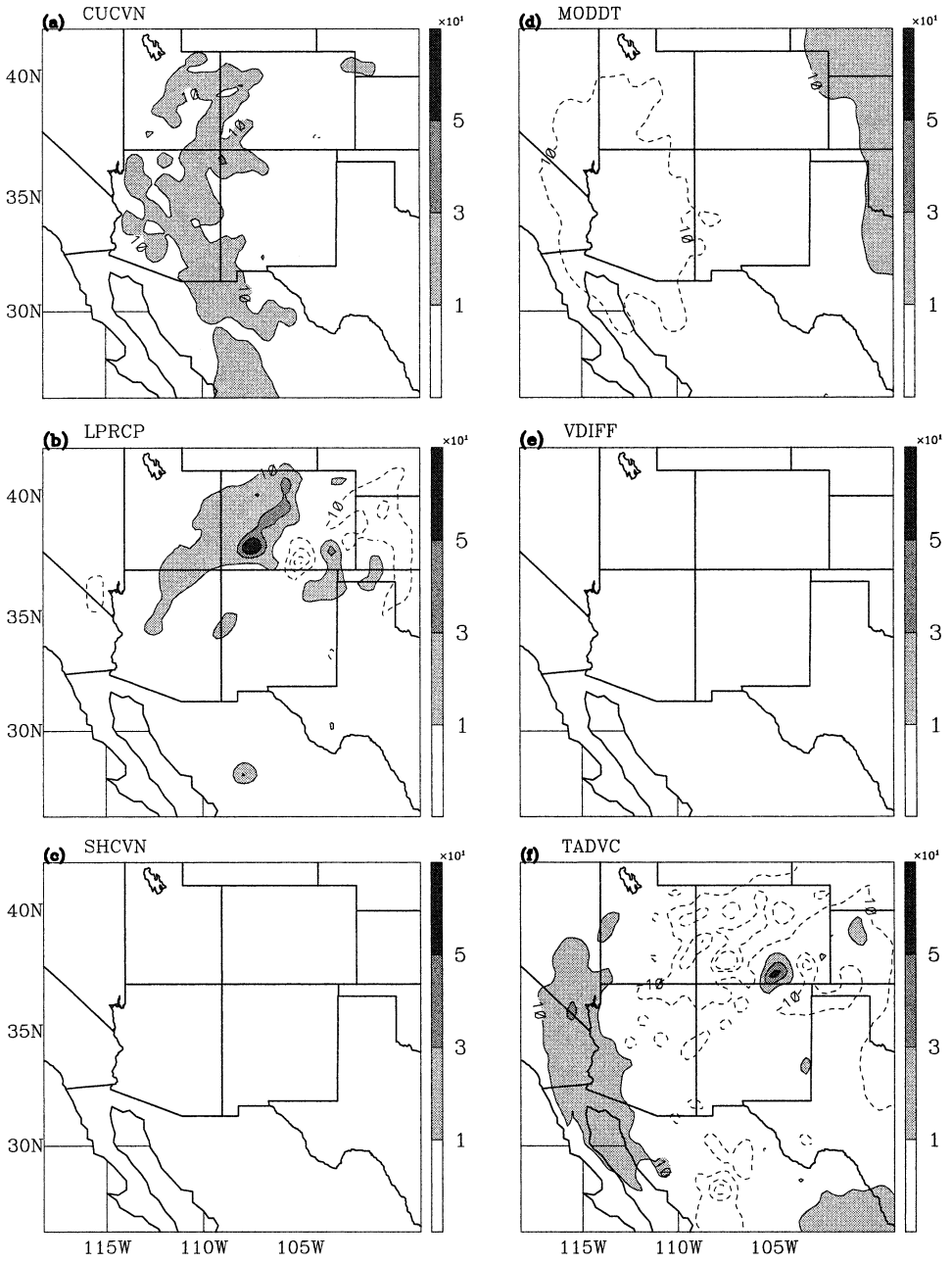

FIG. 6. Weighted covariance map of vertically integrated RSM diagnostic moisture tendency terms for the first canonical factor. Shading interval is 20×10^{-6} kg m^{-2} s^{-1}; min shading is 10×10^{-6} kg m^{-2} s^{-1}. Positive values are shaded; negative values are dashed. Shown are (a) convective precipitation, (b) large-scale precipitation, (c) shallow convective precipitation, (d) moisture tendency, (e) vertical diffusion moisture divergence, and (f) large-scale total moisture divergence.

$\sqrt{92}$, such that the resulting values have units equal to that of the dependent anomaly field. In addition, because of the nature of the normalization used for the time series (i.e., they are normalized such that their inner product, as opposed to their variance, is unity), the resulting quantity is also equal to the correlation coefficient for a linear model of the budget terms. These weighted covariance (or correlation coefficient) maps indicate that most of the anomalous precipitation for this mode is in the form of convective rainfall over the Sierra Madre Occidental and Arizona, with some contribution from large-scale precipitation over Utah and western Colorado. Associated with this precipitation is a drying out of the local atmospheric column and a moistening of the atmosphere over the Great Plains. Of interest, the precipitation regime is not correlated with

any anomalous surface evaporation. Instead the anomalous precipitation is associated with moisture convergence due to large-scale fluxes of water vapor. Although there appears to be some significant negative precipitation associated with this canonical factor (in particular in the large-scale precipitation field), from Fig. 4c it is apparent that this precipitation is not correlated well with the canonical factor (in that r is below 0.4). Therefore we will confine our discussion mainly to the positive patterns of precipitation seen above.

The weighted covariance maps for the second canonical factor of simulated precipitation (Fig. 7) indicate that the anomalous precipitation in the eastern plateau region is due to both increased convective activity and dynamically forced rainfall. As before, there is no anomalous evaporation associated with this precipitation. Instead, the precipitation anomalies are due entirely to increased moisture convergence. From these results then, it is likely that both of the simulated precipitation regimes are related to large-scale dynamic processes (which are influencing the moisture divergence fields) and not directly to land-surface interactions associated with increased evaporation (although these interactions may be indirectly influencing the larger-scale fields).

The results so far have only looked at the full vertical integral of the hydrologic cycle. To examine the vertical structure of this cycle, Figs. 8 and 9 present various profiles of the moisture tendency terms associated with the two precipitation regimes. The first profile in each figure is the seasonal-mean climatology spatially averaged only over those regions with positive precipitation anomalies. To arrive at these values, the climatological profile at each grid point in the domain is calculated. Then, each gridpoint profile is weighted according to the precipitation correlation value found in the respective canonical factor spatial pattern; for grid points with negative correlations, the weighting is set to zero so that these profiles are not included in the average. The weighted profiles are then summed and divided by the sum of the weights of all the profiles included. Hence, weighted area-average profiles of the climatological moisture budget terms are produced.

The second profile is the weighted covariance of the moisture budget terms, again spatially averaged just over those regions with positive precipitation anomalies. Here, instead of using the climatological profiles at each grid point, the weighted ''covariance profiles'' are used; these profiles represent the weighted covariance values at the given levels for a given grid point. As with the first figure, these profiles are then weighted by the gridpoint correlation values of the respective canonical factor map and summed so that a weighted area-average profile can be determined.

The third profile is a composite profile for those days with positive precipitation anomalies (as represented by the canonical factor time series), and the fourth profile is a composite for those days with negative precipitation anomalies. For these profiles, only the positive or negative values (for the third and fourth profiles, respectively) of the normalized time series for each canonical factor are used to weight the gridpoint hydrologic budget time series. At each grid point, the weighted values are then summed over time and divided by the sum of the time series values themselves (again only using the positive or negative values). Hence one arrives at a ''composite profile'' for each grid point, in which the profile represents a composite weighted by the magnitude of the events as determined by the time series of the canonical factor. As with the first figure, these gridpoint profiles are then weighted by the correlation values of the respective canonical factor map so that a weighted area-average profile can be determined.

In a qualitative sense, the first profile gives an indication of the climatological hydrologic balance for only the precipitating regions associated with each mode. The second profile presents the anomalous hydrologic terms correlated with anomalous precipitation over these regions. The third profile shows the full hydrologic balance for periods during which precipitation is occurring in the region, and the fourth profile gives the full hydrologic balance for periods in which there is no precipitation in the region. The reason for the various profiles will become apparent as the discussion continues. These profiles are plotted with respect to kilometers above ground level to account for large changes in elevation over the precipitating regions that preclude averaging along pressure levels. In addition, these are presented as a tendency (kg kg^{-1} s^{-1}) and not moisture convergence (kg m^{-2} s^{-1}) because of the difficulty in calculating the pressure tendency contribution at the various levels; results are qualitatively similar if the tendency terms are scaled by the pressure, which represents an approximation to the full moisture convergence terms.

From Fig. 8, the climatological profile for the western plateau regime (Fig. 8a) indicates a typical seasonal balance for an area of convective precipitation. There is strong low-level large-scale convergence balanced by vertical eddy divergence associated with convective lofting. At approximately 1 km, the two terms switch sign, indicating an outflow of moisture associated with the convective activity. In the region of maximum convective precipitation (approximately 3 km), there is an associated maximum in moisture convergence associated with the vertical diffusion term. The large-scale precipitation is balanced both by vertical diffusion of moisture and by the large-scale moisture convergence. The largest source term above 1 km is the vertical diffusion term, indicating that on a climatological scale most of the precipitation is fed by eddy activity.

However, in examining the weighted covariance profiles associated with the time series for the first mode of precipitation, it is interesting to note that the anomalies related to vertical diffusion are small and are in fact positive for certain levels of anomalous precipitation. Instead, it appears that both the convective and

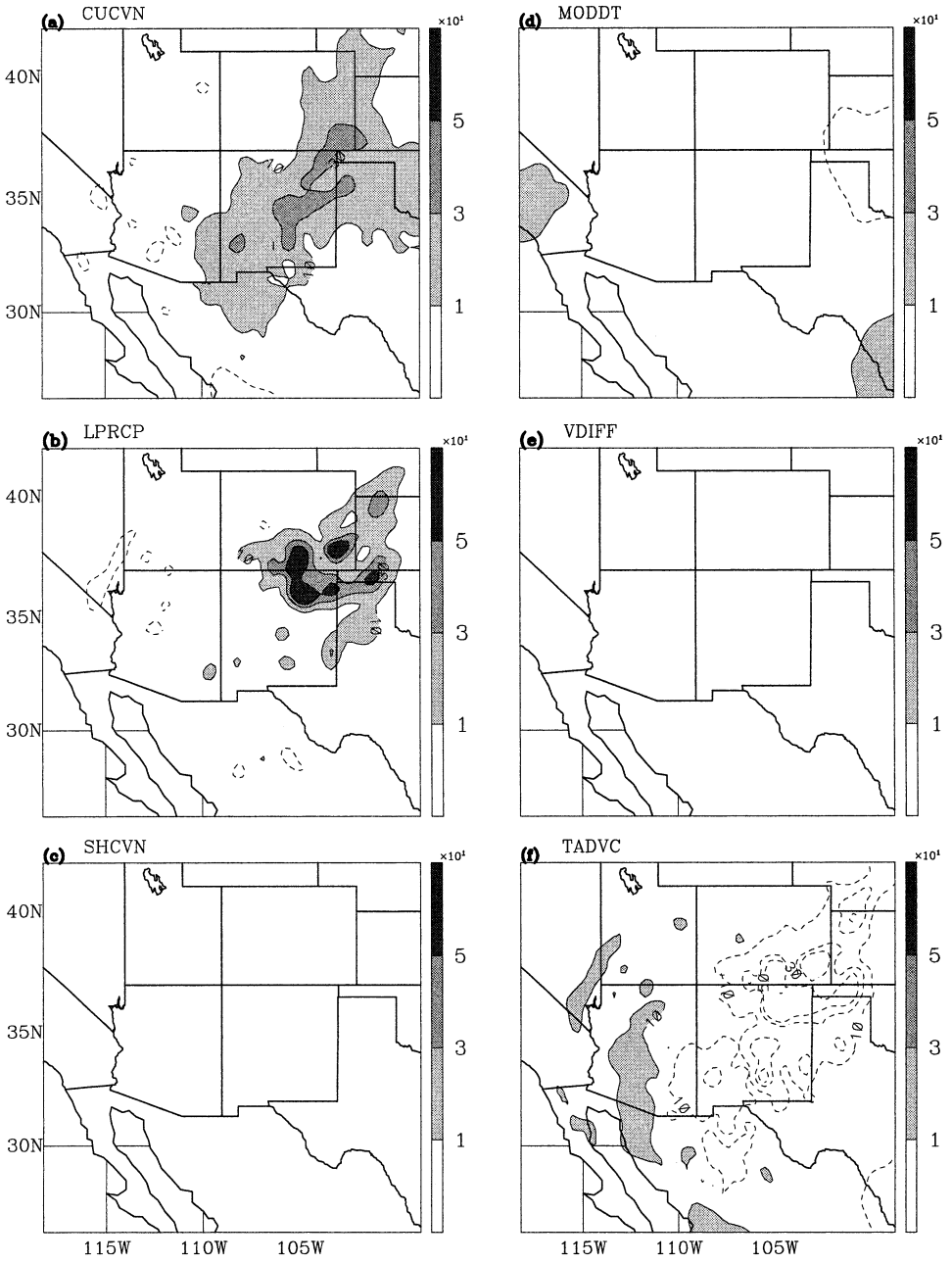

FIG. 7. Same as Fig. 6, but for the second canonical factor.

dynamic precipitation anomalies (whose maximums lie at approximately 3 km) are fed by anomalous large-scale moisture convergence at that level, in agreement with the covariance maps seen earlier.

The discrepancy can be explained by examining the composite profiles associated with periods of precipitation (Fig. 8c) and quiescent activity (Fig. 8d). In both cases, the vertical diffusion profiles are very similar, with low-level divergence feeding convergence between 1 and 3 km; there is slightly more convergence at 2 km associated with precipitating events, and slightly more convergence aloft (approximately 4 km) associated with the nonprecipitating events. When the covariance is calculated, these two terms cancel one another. Hence, the lack of an anomalous vertical diffusion signal associated with precipitation anomalies is due to the fact that the region of interest has large vertical eddy fluxes of moisture occurring at all times (resulting in the large signal seen in the climatology).

The low-level moisture convergence profiles also both show similar structure below 2 km, with low-level convergence through 1 km and divergence from 1 to 2

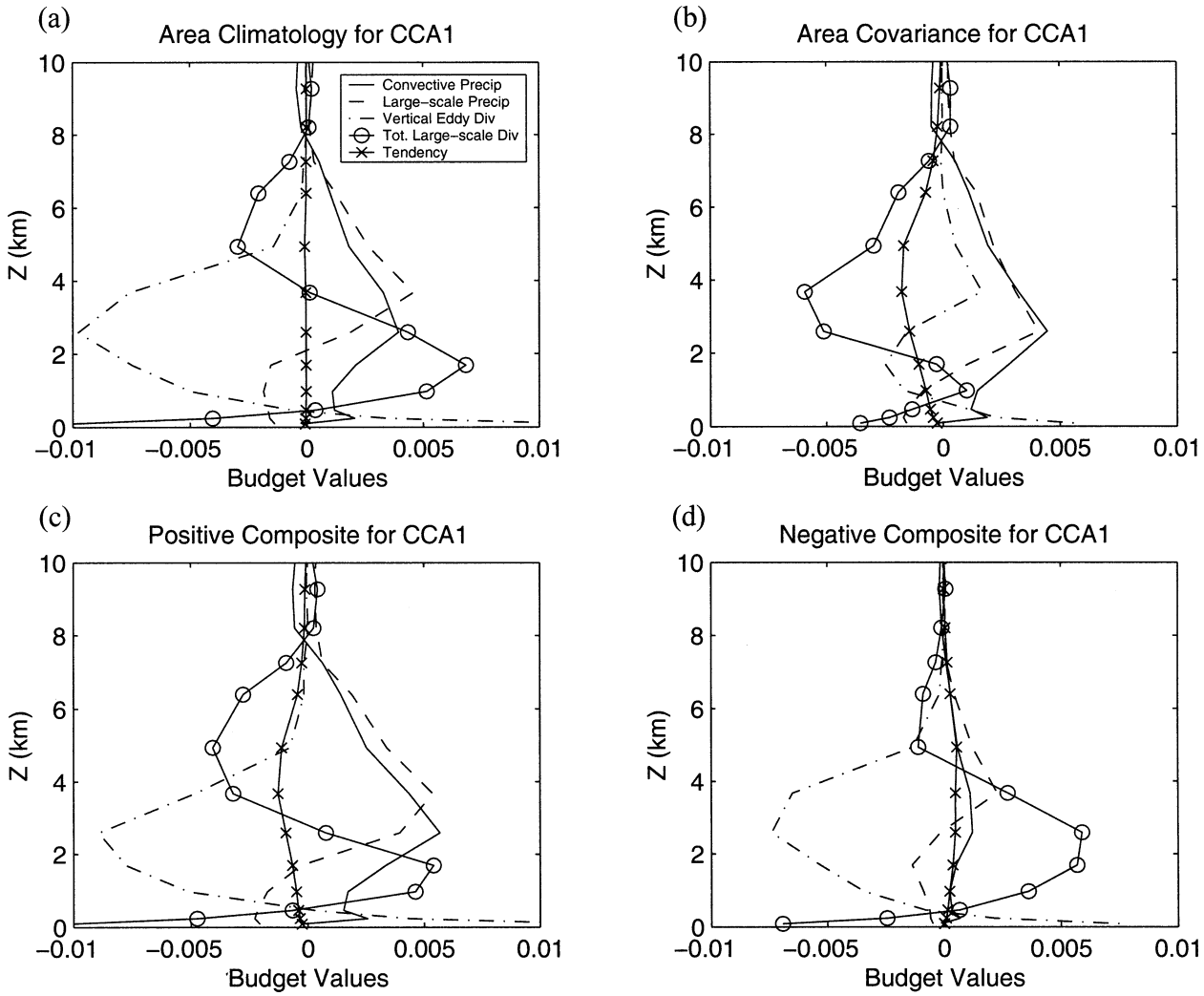

FIG. 8. (a) Area-averaged seasonal-mean profiles of the atmospheric moisture tendency (10^{-6} kg kg^{-1} s^{-1}) terms for the first canonical factor. Area-averaging was done over the region of positive precipitation correlations as seen in Fig. 3c. Terms shown include convective precipitation (solid line), large-scale precipitation (dashed line), vertical diffusion of moisture (dash–dot line), total large-scale moisture divergence (circles), and tendency (crosses). Positive values represent divergence and negative values represent convergence; moisture tendency is given by the respective sign. (b) Same as (a), but for the area-averaged covariance profiles of the moisture tendency terms. (c) Same as (a), but for the area-averaged composite profiles for precipitating days. (d) Same as (a), but for the area-averaged composite profiles for nonprecipitating days. See text for details.

km. However, above 2 km, the two profiles differ significantly. During precipitating events, there is large moisture convergence between 3 and 8 km that is not seen during the nonprecipitating periods. This large-scale convergence, combined with the convergence associated with the quasi-stationary vertical diffusion term, balances the two precipitation terms. During nonprecipitating events, given the same vertical diffusion of moisture but absent the large-scale convergence at upper levels, the precipitation fields are both small and the vertical diffusion is instead balanced by strong large-scale divergence at midlevels. Hence, both convective fluxes of moisture and large-scale advective fluxes of moisture feed the precipitation over the western-plateau region; however, this precipitation may be predicated upon the introduction of the advective fluxes at the upper levels.

When examining the vertical profiles for the eastern-plateau precipitation regime (Fig. 9), we see much the same results. From the climatological profiles, it is likely that the precipitation in this region is largely fed by vertical eddy fluxes of moisture. However, the weighted covariance plot indicates that anomalous precipitation is associated again with large-scale convergence of moisture at around 4 km. As before, the two composite plots indicate that convective activity associated with the vertical diffusion term is similar during both precipitating and nonprecipitating periods; however, the large difference between the two periods arises in the introduction of a large-scale moisture convergence term

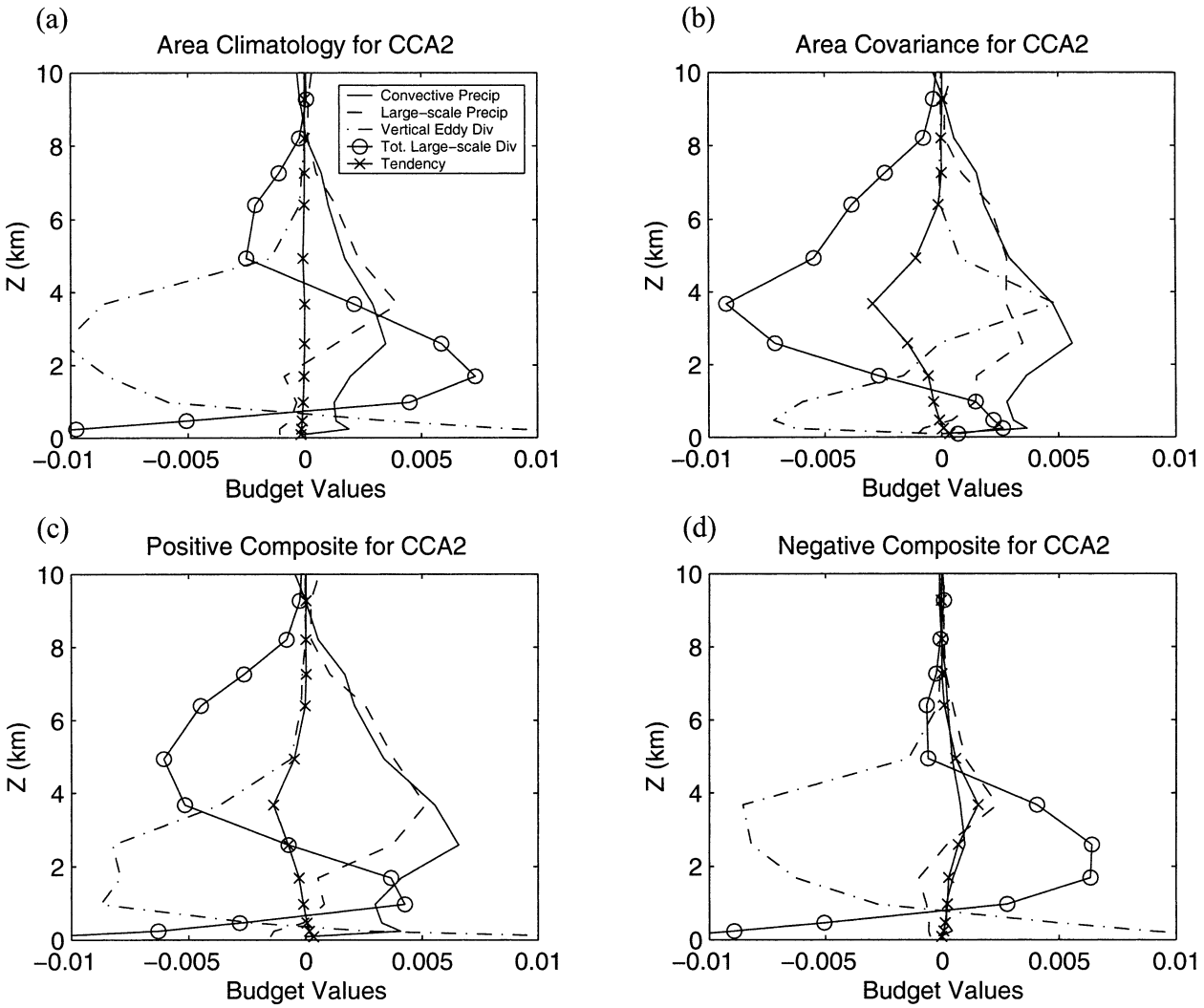

FIG. 9. Same as Fig. 8, but terms for the second canonical factor. Area-averaging was done over the region of positive precipitation correlations as seen in Fig. 4c.

at approximately 5 km, resulting in positive profiles for both convective and large-scale precipitation.

From these results, it is likely that the simulated precipitation patterns are predicated upon the introduction of a large-scale convergence of moisture in the midtroposphere. To determine whether this midtropospheric moisture convergence is due to the horizontal or vertical advection of moisture, the vertical profile of the total convergence term is decomposed into its horizontal and vertical components (which are actually archived separately by the modeling system and hence are consistent with the dynamic forcing within the model).

The climatology, weighted covariance, and precipitating and nonprecipitating composite profiles are again calculated for the precipitating regions of each regime (Figs. 10, 11). For the western-plateau regime (Fig. 10), it can be seen that, in climatologic terms, the total convergence aloft (>4 km) is due both to the horizontal and vertical convergence of moisture; at lower levels, the strong climatological divergence of moisture is due mainly to horizontal advection of moisture from the region. When one looks at the covariance of these terms with the precipitation time series (Fig. 10b), however, it is apparent that *anomalous* total convergence above 4 km is due predominantly to anomalous vertical fluxes of moisture accompanied by a weak anomalous horizontal divergence of moisture; at lower levels, there is an additional contribution to the anomalous total moisture convergence from the horizontal advection of moisture. When comparing the composite plots for precipitating and nonprecipitating events (Figs. 10c,d), it is noticed that this region of low-level anomalous horizontal moisture convergence is indicative of a decrease in the horizontal *divergence* term between 2 and 4 km, which actually remains positive during both precipitating and nonprecipitating events (above 4 km there is

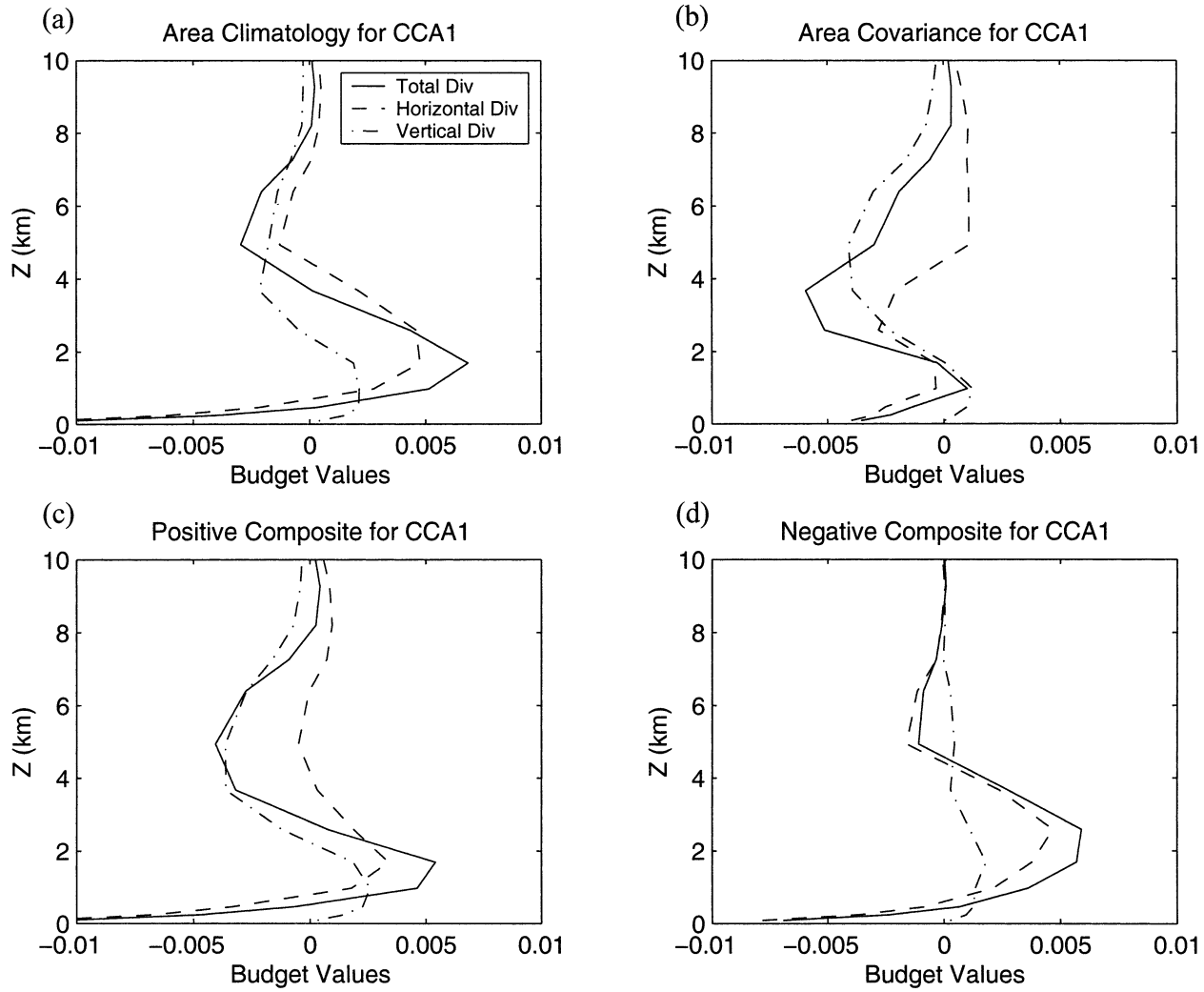

FIG. 10. (a) Area-averaged seasonal-mean profiles of the large-scale moisture divergence (10^{-6} kg kg^{-1} s^{-1}) terms for the first canonical factor. Area-averaging was done over the region of positive precipitation correlations as seen in Fig. 3c. Terms shown include total large-scale moisture divergence (solid line), horizontal moisture divergence (dashed line), and vertical moisture divergence (dash–dot line). Positive values represent divergence; negative values represent convergence. (b) Same as (a), but for the area-averaged covariance profiles of the moisture divergence terms. (c) Same as (a), but for the area-averaged composite profiles for precipitating days. (d) Same as (a), but for the area-averaged composite profiles for nonprecipitating days. See text for details.

actually a consistent horizontal convergence of moisture during both precipitating and nonprecipitating events: hence, the weak positive anomaly signal seen in the covariance plots). However, for the vertical advection term, there is a dramatic switch from vertical divergence during nonprecipitating events to vertical convergence during precipitating events. This result suggests that anomalous precipitation over this region is fed by an anomalous large-scale vertical flux of moisture that augments the climatological convergence associated with local diffusion.

This same process is seen even more dramatically for the eastern-plateau precipitation regime (Fig. 11). In climatologic terms, over this region, low-level moisture divergence is associated with the horizontal advection term, whereas most of the total moisture convergence aloft is due to large-scale vertical fluxes. In addition, covariance with precipitating events indicates that the anomalous total convergence is dominated by anomalies in the vertical component. As with the western-plateau regime, these large vertical convergence anomalies are mirrored in the difference between the composite plots for precipitating and nonprecipitating periods. These indicate a dramatic increase in the vertical moisture convergence aloft during precipitating periods. In this case, however, there is a horizontal divergence between 1 and 6 km in both composites, with very little horizontal convergence of moisture above that, suggesting that precipitation in this region is fed almost purely by local sources, that is, by the vertical advection and vertical

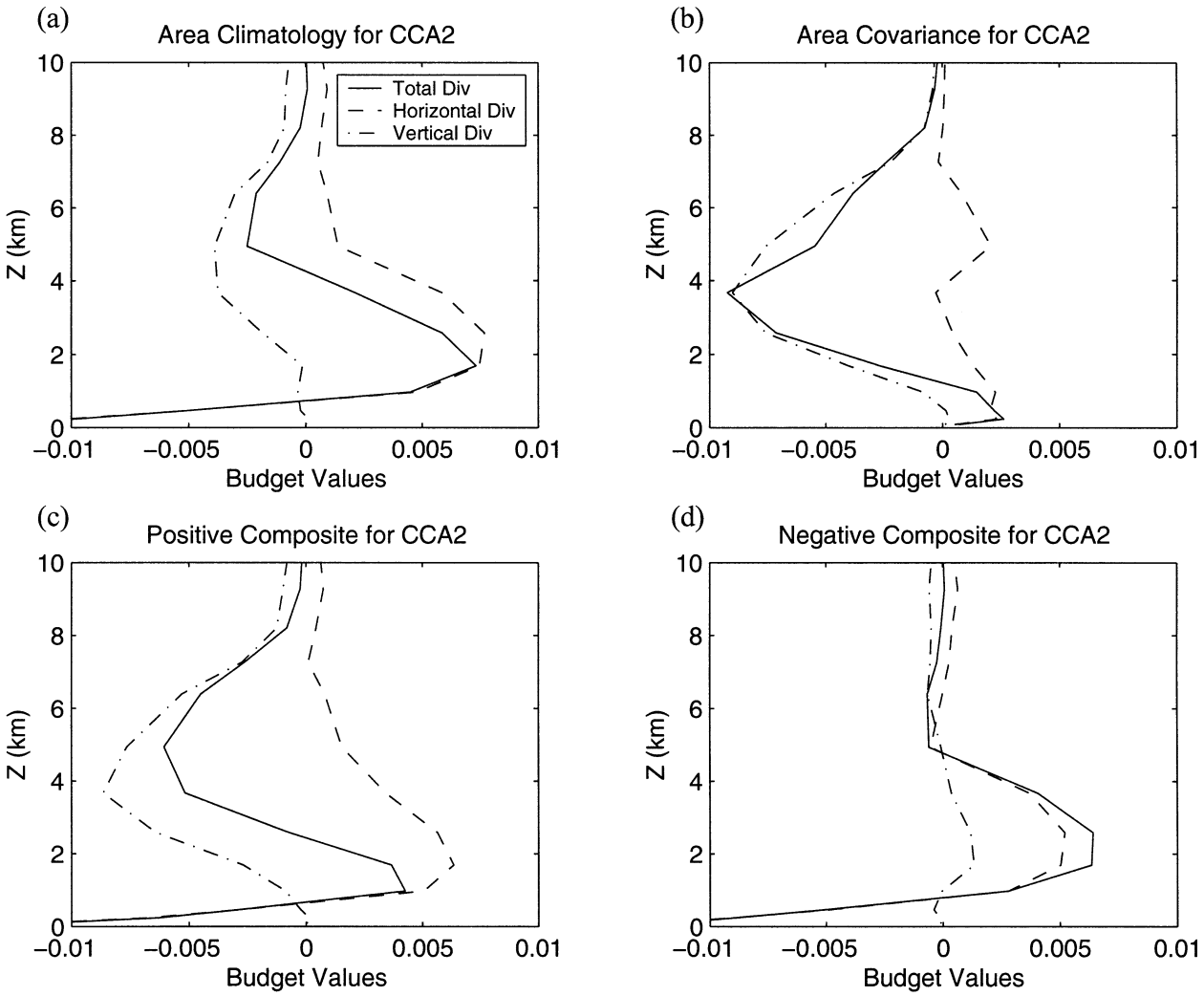

FIG. 11. Same as Fig. 10, but terms for the second canonical factor Area-averaging was done over the region of positive precipitation correlations as seen in Fig. 4c.

diffusion of surface and low-level moisture. This low-level moisture may be advected from remote sources, as suggested by the low-level horizontal convergence composite term; however, it is important to note that this low-level horizontal convergence shows little correlation with the precipitation time series (see Fig. 11b), indicating that the anomalous vertical moisture convergence is drawing moisture from the climatological moisture field and not from anomalous moisture sources.

In general, these results suggest that simulated precipitation over this region is due to the large-scale vertical advection of moisture within the precipitating region, possibly because of the modification of the mid-tropospheric vertical velocities associated with the large-scale monsoon circulation. Previous research has investigated the large-scale dynamic fields corresponding to the precipitation regimes presented here (AR). In general, it is found that precipitation over both the western and eastern portions of the plateau is associated with an anomalous upper-level trough over the midlatitude eastern Pacific and an anomalous ridge over the central United States representing a southward and eastward displacement of the monsoon ridge, in agreement with previous findings (e.g., Carleton 1986). The southward and eastward displacement of the monsoon ridge results in southwesterly flow over the precipitating regions. From quasigeostrophic theory, this southwesterly flow, positioned over the semipermanent monsoon surface low centered on the Rocky Mountain plateau, produces large-scale vertical motion in this region via the differential advection of relative vorticity associated with the pressure centers (AR). These results are in agreement with the hydrologic studies presented here, which indicate that the simulated precipitation events in both regions are predicated upon the introduction of anomalous upper-air ($>$4 km) large-scale moisture convergence, due primarily to the anomalous large-scale vertical fluxes of moisture. Taken together, these results

suggest that the two precipitation regimes identified here are strongly forced by large-scale midlatitude midtropospheric dynamics, which produce anomalous large-scale vertical motions over the precipitating regions. It is the associated anomalous vertical flow of moisture, augmented by the climatological eddy fluxes, that supports precipitation over the two regions.

It unfortunately is extremely difficult to evaluate the simulated moisture budget terms presented here. One way to do so is to use the vertical profiles of wind speed and moisture taken from radiosonde stations that approximately encircle the precipitating region of the western-plateau and eastern-plateau regimes. From these it is possible to produce moisture flux estimates that then can be used to calculate the large-scale horizontal moisture divergence term via a simple line integral. Daily anomalies of these divergence estimates at each level can be correlated with the normalized precipitation time series of each regime to calculate correlation profiles for the horizontal moisture divergence, which then can be compared with the area-average gridpoint divergence values taken from the moisture tendency terms (not shown). In general, there is only weak agreement between the two profiles. In particular, the observations show significantly correlated moisture divergence above 700 mb while those from the simulations are not as large (and are not likely significant), although they do tend to be positive above 600 mb, particularly for the first canonical mode. These discrepancies in the profiles most likely arise from a number of imperfect assumptions in the estimate calculations, including poor vertical resolution of the radiosonde estimates, the influence of intervening topography, and the nature of the quantities being compared [i.e., station-based large-scale flux divergence calculations and area-averaged dynamically based gridpoint gradient calculations (Trenberth 1995)]. However, if the same line-integral technique for estimating area-average horizontal moisture divergence is applied to both the observed and *simulated* profiles (at collocated grid points), there is very good agreement between the simulated and observed estimate values for both regimes (not shown). These results suggest that the model is properly simulating not only the increased precipitation in these regions (as shown here and in AR) but also the observed large-scale upper-level moisture outflow associated with the large-scale wind and moisture fields.

4. Summary

Using 3 months of regional model simulation data for the summer of 1999, it was possible to describe the intraseasonal variability of the atmospheric hydrologic cycle associated with two spatiotemporal precipitation regimes over the southwestern United States. The first precipitation regime is associated with rainfall anomalies predominantly over eastern Utah and western Colorado, with additional anomalies over the Sierra Madre Occidental and eastern Arizona. Vertically integrated moisture budget terms suggest that synoptic-scale precipitation events are predicated upon anomalous large-scale convergence of upper-level moisture over the precipitating region, which augments the quasi-steady moisture convergence produced by vertical diffusion to balance the moisture divergence associated with rainfall during the events. It interestingly does not appear that these events are related to significant *changes* in the vertical diffusion of moisture and hence do not appear to be related to changes in the local land–atmosphere boundary conditions. Instead, the anomalous upper-level moisture convergence associated with these events is most strongly related to anomalous large-scale vertical moisture fluxes combined with a weakening of the horizontal divergence at lower levels (~2–4 km).

The second precipitation regime is characterized by rainfall anomalies over the eastern portion of New Mexico and Colorado. Associated with these anomalies is again an anomalous large-scale moisture convergence term with little signal seen in the eddy diffusion of moisture. However, as with the western precipitation regime, the full precipitation field is balanced by both the (anomalous) convergence term and the (quasi-steady) vertical diffusion term. As before, the large-scale convergence is dominated by the vertical moisture flux component with large vertical convergence occurring during precipitating events and small vertical divergence during nonprecipitating periods. In conjunction with the results for the western-plateau regime, these findings suggest that intraseasonal variability in precipitation over the southwestern United States is strongly modulated by large-scale, midtroposphere dynamics and not simply by local mesoscale activity, in agreement with previous studies (Carleton 1986; Stensrud et al. 1995; Maddox et al. 1995; Mo 2000). Further, it is likely that it is large-scale vertical velocities, arising from the interaction of these midtropospheric dynamics with low-level monsoon pressure patterns over the Rocky Mountain plateau (AR), that produce the large-scale moisture convergence needed to support intraseasonal precipitating events in the region.

It is recognized that the precipitation regimes isolated here, and their related dynamics and hydrodynamics, represent only those regimes that were prevalent during the 1999 summertime season and that additional regimes may be more pronounced during other years. Analysis of 20 yr of observed data for this region suggests that indeed there are additional modes of intraseasonal variability that are not captured in this 1-yr subset; however, the two that are presented here are robust from year to year and do represent a predominant component of the observed intraseasonal variability in this region. Characterization and analysis of additional regimes will be part of future research incorporating multiyear simulations and observations.

Acknowledgments. The author is especially grateful to Dr. John Roads and Jack Ritche of Scripps Institution of Oceanography for providing the model simulation data used throughout this paper and for their insightful comments made during the preparation of this manuscript. This research was funded by Cooperative Agreement NOAA-NA16GP1622. The views expressed herein are those of the author and do not necessarily reflect the views of NOAA.

APPENDIX

Regional Spectral Modeling System

The NCEP global to regional modeling system used in this study contains two components—a low-resolution global spectral model and a regional spectral model with a single nest. The nesting method is a one-way, noninteractive procedure that is designed to calculate regional responses (or adjustments) of the RSM to the large-scale background fields provided by the coarser-resolution GSM. This nesting procedure is performed through the entire domain, not only at the lateral boundary zones, and is therefore referred to as a perturbation method [see Juang and Kanamitsu (1994) and Juang et al. (1997) for details].

The GSM and RSM use the same primitive hydrostatic sigma-coordinate equations expressed in slightly different forms (Juang and Kanamitsu 1994; hereinafter JK). The GSM equations consist of the vorticity, divergence, virtual temperature, and conservation equation for water vapor on 18 sigma-layer coordinates and a mass continuity equation for surface pressure (Kanamitsu 1989). The regional model differs slightly in that it utilizes the momentum equations instead of the vorticity/divergence equations (JK). The model physics were described in Kalnay et al. (1996). The following are some of the important parameterizations:

Deep convection: Deep convection is modeled using a simplified Arakawa–Schubert parameterization (Kalnay et al. 1996). This scheme assumes a quasi-equilibrium available buoyant energy; changes in buoyant energy associated with convective activity are provided by large-scale changes associated with the environmental stability of the atmosphere. The instability is removed by relaxing the temperature and moisture profiles toward equilibrium values using a prescribed time interval (Grell 1993). In the simplified version, cloud size is effectively prescribed as opposed to being determined from a parameterization-dependent spectrum. In addition, Hong and Pan (1996) detail modifications to this scheme. In particular, in the subcloud layers, the level of maximum moist static energy represents the level of origination for updraft air; however, if the depth between this level and the level of free convection is greater than a certain threshold, convection is suppressed. Convection can also be produced in regions with large convective available potential energy (Hong and Pan 1996). It is important that the scheme accounts for downdrafts associated with convection; in previous modeling attempts over the southwest United States, it was shown that the parameterization scheme needs to consider evaporation of precipitation below the cloud base in order to create outflow and increased convection in the southwestern United States (Dunn and Horel 1994).

Large-scale precipitation: A vertical iteration starting from the top sigma level checks for supersaturation at each level. Supersaturated layers are set to a near-saturated state using an approximate wet-bulb process; all excess liquid water goes into the form of precipitation. As the precipitation moves downward through the column, it is either augmented (by passage through additional supersaturated layers) or reduced (by passage through unsaturated layers). If it is reduced by passage through unsaturated layers, evaporation in that layer occurs, with the rate of evaporation dependent upon the drop size distribution (NOAA/NMC Development Division 1988).

Boundary layer processes: Boundary layer processes (Hong and Pan 1996) are based upon a nonlocal boundary layer vertical diffusion in which the surface layer and boundary layer are coupled using a prescribed profile with similarity-based scale parameters. Included in this scheme are also countergradient diffusion processes, which are shown to be important for mixing low-level moisture upward more efficiently (Hong and Pan 1996). It is important that the scheme strongly couples the boundary layer physics and the convective processes described earlier, improving the precipitation forecasts for heavy rain events (Hong and Pan 1996). Boundary layer height is computed iteratively by first computing the boundary height without accounting for virtual temperature instability near the surface; from this estimate, calculations of vertical velocities can be obtained, which then allow estimation of the virtual temperature instability and subsequently modified PBL heights (Hong and Pan 1996). The diffusion parameters for momentum and mass can then be determined from the boundary layer height using the prescribed profile shape. Above the boundary layer, vertical eddy transfer uses a more traditional Richardson number–dependent diffusion process.

Soil model processes: The soil model in the RSM is based upon the Oregon State University scheme as described in Chen et al. (1996). The scheme includes an explicit vegetation canopy, soil hydrologic processes, and soil thermodynamics. For the soil scheme, it uses a two-level (0.1- and 1.9-m thick) prognostic soil model for both moisture and temperature, with parameterized diffusion between

the two levels and a spatial distribution of soil type and soil properties as described in Betts et al. (1997). Also included in the prognostic scheme are equations for moisture contained in vegetation and snow (Chen et al. 1996). Evaluation and analysis of the soil model performance has been done both within the NCEP Eta (Chen et al. 1996; Betts et al. 1997) and RSM (Roads and Chen 2000) modeling systems.

For the horizontal spectral representation, the GSM uses a triangular-62 (T62) truncation of the spherical harmonics as the basis functions. The regional model expresses the prognostic model variables in terms of the specified large-scale fields and their perturbations on sigma surfaces. The regional model perturbations use trigonometric functions as their basis functions; in particular cosine–cosine basis functions are used for all perturbations except the zonal momentum perturbation, which uses sine–cosine functions, and the meridional momentum perturbation, which uses cosine–sine functions (see JK for details). All nonlinear dynamic and physical terms are computed in gridpoint space for both. The RSM perturbation tendencies are forced to zero at the regional lateral boundaries by a relaxation toward the external boundary. Semi-implicit time integration is subsequently performed to suppress the higher-frequency waves and to allow the use of a longer time step.

The nesting method itself is a one-way, noninteractive procedure designed to calculate regional perturbations (or adjustments) of the RSM to the large-scale background fields provided by the coarser-resolution GSM. For this research, a 92-day simulation is performed, initialized at 0000 UTC 1 July 1999. The nesting method begins by first using daily 0000 UTC NCEP global reanalysis data as initial conditions for a 24-h GSM integration; model output is archived every 6 h. The linearly interpolated GSM field taken between two consecutive output times is used as the base field for the RSM forecast. Interpolation of the GSM data from the global to regional grid is done directly using a spectral-to-gridpoint conversion of the global fields. As pointed out by Juang et al. (1997), it is important to include the GSM integration to avoid large-scale perturbation growth that results when using just the reanalysis base fields. Because all surface initial conditions for the RSM except for orography are provided by the coarser GSM, the sea surface temperature in the Gulf of California, which is absent from the global data, is assigned a constant value equal to the temperature at the mouth of the gulf (approximately 29°C). This assignment is based upon results of previous modeling studies that indicated the importance of proper SST fields in the gulf (Dunn and Horel 1994); sensitivity studies indicate that finer-scale SST resolution does not quantitatively affect the dynamic fields in the region (Anderson 1998).

To produce a continuous 92-day simulation of the RSM (as opposed to a set of 92 24-h weather forecasts), the coarse-scale GSM and finescale RSM short-term forecast fields at 2400 UTC (and not the reinitialized 0000 UTC GSM field) are used as the initial conditions for the next RSM nesting period. In terms of numerics, this technique allows the RSM forecast, which inherently contains corrections for anomalies associated with enhanced orography and resolution, to carry these corrections forward from one nesting period to the next, thereby reducing spinup effects. Regional surface prognostic fields, however, are not reinitialized and represent a continuous forecast simulation.

REFERENCES

Anderson, B. T., 1998: Investigation of summertime low-level winds over the Gulf of California and the southwestern United States. Ph.D. thesis, University of California, San Diego, 176 pp.

——, and J. O. Roads, 2002: Regional simulation of summertime precipitation over the southwestern United States. *J. Climate,* in press.

——, ——, and S.-C. Chen, 2000a: Large-scale forcing of summertime monsoon surges over the Gulf of California and southwestern United States. *J. Geophys. Res.,* **105** (D19), 24 455–24 467.

——, ——, ——, and H.-M. H. Juang, 2000b: Regional simulation of the low-level monsoon winds over the Gulf of California and southwestern United States. *J. Geophys. Res.,* **105** (D14), 17 955–17 969.

Berbery, E. H., 2001: Mesoscale moisture analysis of the North American monsoon. *J. Climate,* **14,** 121–137.

Berg, W. K., D. M. Anderson, and J. J. Bates, 2000: Satellite observations of a Pacific moisture surge associated with flooding in Las Vegas. *Geophys. Res. Lett.,* **27,** 2553–2556.

Betts, A. K., F. Chen, K. E. Mitchell, and Z. I. Janjic, 1997: Assessment of the land surface and boundary layer models in two operational versions of the NCEP Eta Model using FIFE data. *Mon. Wea. Rev.,* **125,** 2896–2916.

Carleton, A. M., 1986: Synoptic–dynamic character of ''bursts'' and ''breaks'' in the south-west U.S. summer precipitation singularity. *J. Climatol.,* **6,** 605–622.

Chen, F., and Coauthors, 1996: Modeling of land surface evaporation by four schemes and comparison with FIFE observations. *J. Geophys. Res.,* **101,** 7251–7268.

Chen, S.-C., J. O. Roads, H.-M. H. Juang, and M. Kanamitsu, 1999: Global to regional simulations of California wintertime precipitation. *J. Geophys. Res.,* **104,** 31 517–31 532.

Comrie, A. C., and E. C. Glenn, 1998: Principal components–based regionalization of precipitation regimes across the southwest United States and northern Mexico, with an application to monsoon precipitation variability. *Climate Res.,* **10,** 201–215.

Dunn, L. B., and J. D. Horel, 1994: Prediction of central Arizona convection. Part II: Further examination of the Eta Model forecasts. *Wea. Forecasting,* **9,** 508–521.

Grell, G. A., 1993: Prognostic evaluation of assumptions used by cumulus parameterizations. *Mon. Wea. Rev.,* **121,** 764–787.

Hamill, T. M., 1999: Hypothesis tests for evaluating numerical precipitation forecasts. *Wea. Forecasting,* **14,** 155–167.

Hong, S.-Y., and H.-L. Pan, 1996: Nonlocal boundary layer vertical diffusion in a medium-range forecast model. *Mon. Wea. Rev.,* **124,** 2322–2339.

Juang, H.-M. H., and M. Kanamitsu, 1994: The NMC nested regional spectral model. *Mon. Wea. Rev.,* **122,** 3–26.

——, S.-Y. Hong, and M. Kanamitsu, 1997: The NCEP regional spectral model: An update. *Bull. Amer. Meteor. Soc.,* **78,** 2125–2143.

Kalnay, E., and Coauthors, 1996: The NCEP/NCAR 40-Year Reanalysis Project. *Bull. Amer. Meteor. Soc.,* **77,** 437–471.

Kanamitsu, M., 1989: Description of the NMC global data assimilation and forecast system. *Wea. Forecasting,* **4,** 335–342.

Kiladis, G. N., 1999: Dynamics of intraseasonal rainfall variability during the North American monsoon season. *Proc. 24th Annual Climate Diagnostics and Prediction Workshop,* Tucson, AZ, NOAA Climate Prediction Center, 43–44.

Maddox, R. A., D. M. McCollum, and K. W. Howard, 1995: Large-scale patterns associated with severe summertime thunderstorms over central Arizona. *Wea. Forecasting,* **10,** 763–778.

Mamassis, N., and D. Koutsoyiannis, 1996: Influence of atmospheric circulation types on space–time distribution of intense rainfall. *J. Geophys. Res.,* **101,** 26 267–26 276.

Mo, K. C., 2000: Intraseasonal modulation of summer precipitation over North America. *Mon. Wea. Rev.,* **128,** 1490–1505.

Mullen, S. T., J. T. Schmitz, and N. O. Renno, 1998: Intraseasonal variability of the summer monsoon over southeast Arizona. *Mon. Wea. Rev.,* **126,** 3016–3035.

NOAA/NMC Development Division, 1988: Documentation of the NMC global model, 244 pp. [Available from NOAA/NCEP Environmental Modeling Center, 5200 Auth Rd., Washington, DC 20233.]

Petersen, W. A., and S. A. Rutledge, 1998: On the relationship between cloud-to-ground lightning and convective rainfall. *J. Geophys. Res.,* **103,** 14 025–14 040.

Roads, J. O., and S.-C. Chen, 2000: Surface water and energy budgets in the NCEP regional spectral model, *J. Geophys. Res.,* **105,** 29 539–29 550.

Schmitz, J. T., and S. L. Mullen, 1996: Water vapor transport associated with the summertime North American monsoon as depicted by ECMWF analyses. *J. Climate,* **9,** 1621–1634.

Staudenmaier, M., 1996: Precipitation verification statistics from the NCEP Operational Model Suite. NCEP Western Regional Tech. Attachment 96-28, 11 pp. [Available online at http://www.wrh.noaa.gov/wrhq/96TAs/TA9628/ta96-28.html.]

Stensrud, D. J., R. L. Gall, S. L. Mullen, and K. W. Howard, 1995: Model climatology of the Mexican monsoon. *J. Climate,* **8,** 1775–1793.

Trenberth, K. E., 1995: Truncation and use of model-coordinate data. *Tellus,* **47,** 287–303.